
Ocean surface current retrieval from space: The Sentinel-2 multispectral capabilities

Yurovskaya Maria ^{1,2,*}, Kudryavtsev Vladimir ^{1,2}, Chapron Bertrand ^{2,3}, Collard Fabrice ⁴

¹ Marine Hydrophysical Institute of RAS, Sevastopol, Russia

² Satellite Oceanography Laboratory, Russian State Hydrometeorological University, Saint Petersburg, Russia

³ Institut Français de Recherche pour l'Exploitation de la Mer, Plouzané, France

⁴ OceanDataLab, Déolen, France

Maria Yurovskaya, email address : mvkosnik@gmail.com

Abstract :

The Sentinel-2 MultiSpectral Instrument (MSI) collects multiple spectral band images, corresponding to specific sensing wavelengths and spatial resolutions, i.e. 10 m, 20 m and 60 m, respectively. Images are collected one at the time with a given time-lag between observations. Under favorable conditions, spatio-temporal characteristics of propagating ocean surface waves can thus uniquely be retrieved. A method for surface current vector field reconstruction is then developed. Demonstrated over different deep ocean regions, the retrieved surface current fields well compare with medium-resolution ocean circulation model or derived-velocities from altimeter measurements. At finer scales, the surface wave-conservation law is recovered, with the associated relationship between current vorticity and wave-ray curvature. Over shallow water regions, the wave propagation properties well follow sea depth variations, consistent with ETOPO1 data. Finally, time-lag between detector bands can also be exploited to estimate speed and direction properties of detected surface wave breaking whitecaps. An analysis of velocity reconstruction errors further reveals that Sentinel-2 MSI inter-channel co-registration is realized with an accuracy better than 0.1 pixel. Overall, these results confirm very promising capabilities of optical imagery to provide direct surface current velocity measurements from space, over relatively large areas, O(100 km), with a spatial resolution down to O(1 km).

Highlights

► A method is developed for surface current reconstruction from Sentinel-2 images ► It is based on cross-spectral phase estimation between images from different bands ► Retrieved current fields well compare with model and altimeter measurements ► Over shallow water regions, sea depth is reconstructed ► Inter-channel time delay is used to estimate speed and direction of large whitecaps

Keywords : Ocean currents, Sea surface optical images, Wave dispersion relation, Time lag, Wave breaking, Sentinel-2, Satellite methods

13 **1. Introduction**

14 An area of unfilled promise in satellite ocean remote sensing is the devel-
15 opment of a direct inversion of upper ocean surface current characteristics.
16 From precise sea level measurements, satellite altimeters greatly help reveal
17 balanced motions to describe large to meso-scale ocean dynamics properties.
18 Indeed, away from the equator, a sea level gradient results as a pressure
19 gradient, to be balanced by the Coriolis force associated to a current flow.
20 This is the geostrophic balance. Altimeter-derived currents thus provide a
21 good representation of large scale depth-integrated currents. However, sur-
22 face currents are certainly not always in geostrophic balance, and also reflect
23 interactions with upper ocean wind and wave motions. Altimeter measure-
24 ments cannot fully capture multi-scale variability of the ocean circulation,
25 especially within the uppermost surface layers, which remains a challenge for
26 theoretical and practical ocean modeling. Techniques using Doppler radar
27 measurements (e.g. Goldstein and Zebker (1987); Chapron et al. (2005);
28 Romeiser et al. (2014); Rodriguez et al. (2018)) can provide more direct
29 measurements, but also face a number of difficulties. Not solely related to

30 platform attitude issues, inversion algorithm definitions must account for de-
31 tected orbital motions of waves, including wave breaking effects (Johannessen
32 et al. (2008); Hansen et al. (2012); Martin and Gommenginger (2017); Martin
33 et al. (2018); Yurovsky et al. (2019)).

34 Overlooked, techniques from photographs and video recordings of the sea
35 surface have long been demonstrated and reported in various field studies
36 (e.g., Barber (1949); Dugan et al. (2001); Dugan and Piotrowski (2003);
37 Leckler et al. (2015); Rasclé et al. (2017); Yurovskaya et al. (2018)). Today,
38 with the significant improvement of optical instruments, like event cameras
39 (Rebecq et al. (2017)), stereo systems (Fedele et al. (2013)) and relatively sim-
40 ple remote controlled measurements from drones (Yurovskaya et al. (2018a);
41 Yurovskaya et al. (2018)), improved spatio-temporal properties of the ocean
42 surface can be readily obtained.

43 From a satellite perspective, optical imagery also provides high resolution
44 sea surface images over large areas. As presently available, an ensemble
45 of satellite missions (e.g. Landsat-8, Sentinel-2a and 2b, RapidEye, among
46 others) not only often enable to distinguish individual ocean surface waves
47 from acquired images, but also provide means to characterize spatio-temporal
48 ocean surface wave displacements. Indeed, the specific viewing geometry of
49 the satellite radiometers offers time-lagged acquisitions for different spectral
50 channels. Near-simultaneous measurements can thus be exploited to estimate
51 local displacements, such as moving objects on the sea surface, river ice
52 debris (Kääb et al. (2013)), ships (Takasaki et al. (1994)), surface wave fronts
53 (De Michele et al. (2012)), but also wave breakers that often manifest in
54 satellite optical images as localized bright events. An overview of motion

55 detection methods from near-simultaneous satellite images is given in Kääb
56 and Leprince (2014).

57 For Sentinel-2 measurements, cross-spectral analysis between images col-
58 lected in two specific bands, was first demonstrated to retrieve surface wave
59 directional properties and current characteristics (Kudryavtsev et al. (2017a,b)).
60 This initial methodology was then further improved to reconstruct the sur-
61 face current velocity vector (Yurovskaya et al. (2018b)). In this present work,
62 the aim is to further test the instrument capabilities, applying the proposed
63 methodology for different cases and over different ocean regions. For deep
64 sea cases, the analysis concentrates on the applicability of the principle of
65 wave action conservation, and more specifically the expected relationship be-
66 tween current vorticity and wave-ray curvature (Kenyon (1971); Quilfen et al.
67 (2018)). Over shallow water regions, changes of wave dispersion properties
68 are then further shown to help reveal sea depth variations. Finally, time-lag
69 between detector bands is further exploited to estimate, from space, speed
70 and direction of detected surface wave breaking whitecaps, key for direct
71 measurements of momentum and gas fluxes.

72 The structure of the paper is as follows. Section 2 introduces Sentinel-
73 2 MSI time-lagged measurements, and the method to retrieve current and
74 bathymetry information. Examples, including whitecap velocities, are given
75 in Section 3. Discussion in Section 4 covers applicability of the proposed
76 approach, possible error sources and estimation of velocity reconstruction
77 accuracy.

78 2. Sentinel-2 MSI data and Methodology

79 2.1. MSI time-lagged data

80 Sentinel-2A and Sentinel-2B multispectral (MSI) instruments are com-
81 posed of 13 spectral bands (443-2190 nm) with different spatial resolutions,
82 ranging from 10 m to 60 m, to cover a swath width of 290 km formed by
83 12 sensor clusters. Due to a specific sensor configuration, i.e. the relative
84 detector alignment, there is a parallax angle between both neighbor clusters
85 and spectral channel sensors inside each cluster. It leads to inter-cluster and
86 inter-band short-time lags that can be estimated from a viewing geometry as

$$dt = D/V$$
$$D = H\sqrt{\tan^2\theta_1 + \tan^2\theta_2 - 2\tan\theta_1\tan\theta_2\cos(\varphi_1 - \varphi_2)}, \quad (1)$$

87 where H is the altitude of the satellite, $\theta_{1,2}$ and $\varphi_{1,2}$ zenith and azimuth
88 view angles of the same point in two different bands, V is the satellite speed
89 and D the length of satellite track. Compared to Eq. (22) by Kudryavtsev
90 et al. (2017a), the absolute satellite speed and flight distance are considered
91 in Eq. (1), instead of ground ones, as the viewing angles are defined from
92 ground to sensor.

93 While this is not critical for an overall estimation of wave dispersion
94 characteristics (Kudryavtsev et al. (2017a,b)), a more precise dt value is
95 essential to best retrieve local velocities, as discussed in Section 4.

96 Values for H and V are calculated from satellite coordinates, given in MSI
97 auxiliary files. The time values for each band and strip (cluster) are also
98 directly listed in metadata information. As tested, both ways to estimate
99 the time lags give similar results, within 1-2% precision. The summary of

100 inter-band and inter-cluster relative time shifts is reported in Fig. 1. The
 101 listed time lags apply for both Sentinel-2A and Sentinel-2B data at different
 102 satellite locations.

103 Time-lagged acquisitions can be employed to infer instant velocity es-
 104 timates. For long enough time delay, a surface drift can be estimated by
 105 tracking detectable features, e.g. surface slicks, as performed by Matthews
 106 and Awaji (2010) and Matthews and Yoshikawa (2012), using 45 s time-
 107 lagged satellite stereo acquisitions. The larger the time lag, the more accu-
 108 rate becomes the motion detection (Kääb and Leprince (2014)). For ocean
 109 surface wave dispersion analysis, the time lag should be shorter, to ensure
 110 high coherency between two consecutive observations. Optimal values can
 111 still amount to several seconds. As estimated for MSI, the longest inter-band
 112 time lag is 2.6 s, obtained for B02 and B09 data. The B09 spatial resolution
 113 (60 m) is too coarse to sufficiently resolve surface waves. For our purpose,
 114 preference is given to a higher resolution channel combination, i.e. bands
 115 B02 and B04 with 1 s time lag.

116 2.2. Current Vector and Ocean Depth Reconstruction

To derive wave dispersion characteristics, the approach follows Kudryavtsev et al. (2017a). Consider I_1 , I_2 , image brightness fragments in B02 and B04, respectively, their coherence and phase spectra are:

$$Coh = \frac{\text{abs}(\hat{I}_1 \hat{I}_2^*)}{\sqrt{\hat{I}_1 \hat{I}_1^* \cdot \hat{I}_2 \hat{I}_2^*}}, \quad (2)$$

$$F = \arg(\hat{I}_1 \hat{I}_2^*), \quad (3)$$

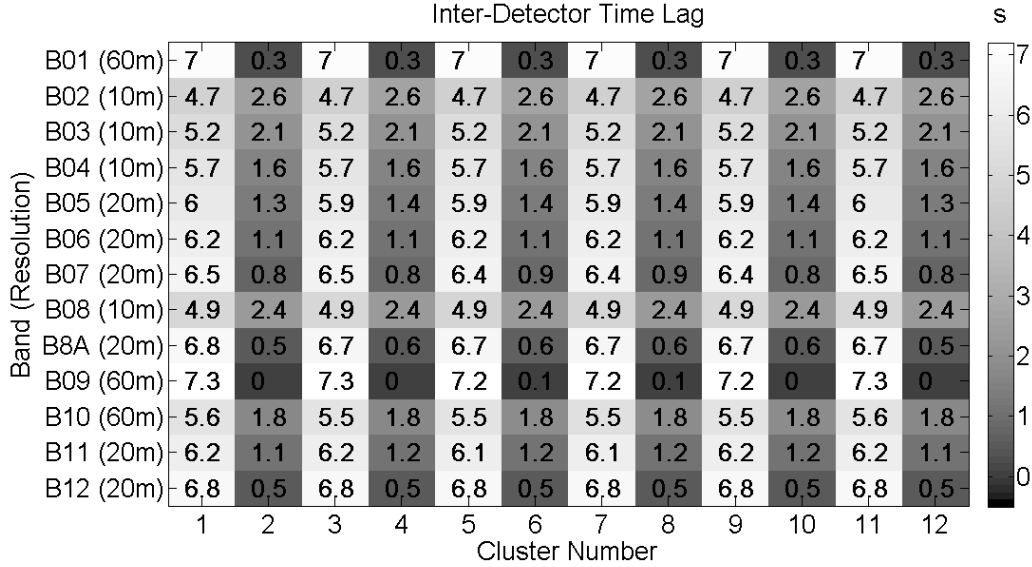


Figure 1: Inter-cluster and inter-band time lag (relative to the earliest acquisition) in MSI Sentinel-2 data.

with $\hat{I}_{1,2}$, Fourier transform, and * its complex conjugation. Following linear surface wave theory, the phase spectrum in absence of current is

$$F_0 = dt\sqrt{gk\tanh(kh)}, \quad (4)$$

where g is gravity, k wavenumber, and h water depth.

In presence of a surface current, the surface wave dispersion is modified. The upper ocean is moving with a current velocity \mathbf{U} , very slowly varying with position, i.e. varying over a scale much larger than the peak wavelength of the wave system, typically from 1 km to 20 km. To first order, this surface current locally, e.g. $O(1 \text{ km})$, Doppler-shifts the phase as:

$$F = F_0 + \mathbf{k}\mathbf{U} \cdot dt. \quad (5)$$

In terms of phase velocity, $C = F/(kdt)$, a transect of the phase spectrum along the wave direction provides an estimate of the corresponding surface current projection, as a measurable deviation between $C(k_j)$ and $C_0(k_j)$:

$$U_j = C - C_0 = F/(kdt) - \sqrt{\tanh(kh)g/k},$$

or for deep sea conditions ($kh \gg 1$):

$$U_j = F/(kdt) - \sqrt{g/k}. \quad (6)$$

117 For deep water conditions or when the ocean depth is known, the inclina-
 118 tion of the plane $(F - F_0)/dt$ in the wavenumber space gives the current
 119 magnitude and direction. In this case Eq. (5) can be solved using the least
 120 square method, over points k_j with coherence (2) exceeding some pre-assigned
 121 threshold value ($coh = 0.8$ in present calculations).

For unknown h , the least square method is unstable. Over areas with detected waves much longer than the water depth ($kh \ll 1$), the problem can reduce to zero current (Eq. (4)) to provide an estimated bathymetry. The longer the waves, the more accurate is this procedure. The analysis now solely concentrates on the peak wavenumber k_p . The time-lagged data is not anymore necessary, as the wave frequency conserves:

$$\sqrt{gk_p \tanh(k_p h)} = const = \sqrt{gk_0},$$

$$h(k_p) = \frac{1}{k_p} \operatorname{atanh} \frac{k_0}{k_p}, \quad (7)$$

122 where k_0 is the wave peak wavenumber in the deep water region.

123 To note, a surface current should not significantly impact the estimated
 124 depth. For a 1 m/s flow, the term \mathbf{kU} is generally much smaller than $k\sqrt{gh}$,
 125 down to 5-10 m water depth.

126 *2.3. Algorithm Implementation*

127 Figure (2) provides the step-by-step algorithm to estimate the projection
128 of the current velocity in the wave propagation direction. To illustrate the
129 methodology, a Sentinel-2 image is considered (Fig. 2, b), acquired August,
130 27th, 2016 at 06:46 in the region of the Somali current. This current is flow-
131 ing from the South, rotating clockwise near the Somali peninsula. This large
132 scale current is generally well captured by altimeter measurements (GlobCur-
133 rent surface current data, www.globcurrent.org), as reported in Fig. 2, a. The
134 current front is further clearly distinguished using MSI optical data, as col-
135 ored waters from the Africa coast are very well delineated. A fragment of the
136 frontal area is shown in Fig. 2, c, with two squared areas of size 1 km x 1 km
137 marked inside (2) and outside (1) the current. Zooming in (Fig. 2, d, h), the
138 detected wavy patterns for these two areas are apparently quite different: a
139 dominant wave system in the upper area, and a more entangled multi-modal
140 wave structure inside the current. The respective coherence fields, Eq. (2),
141 and phase shift spectra, Eq. (3), are shown in subplots (e)-(f) and (i)-(j).
142 Signs of phase spectra indicate the propagation direction of detected wave
143 systems. For clarity, only points with coherence level larger than 0.8 are
144 considered. In our case ($dt > 0$), negative phase shift corresponds to the
145 direction waves are propagating to.

146 The curves $U_j(k)$, using (6) along transects shown on Fig. 2, f, j (dashed
147 lines), are plotted in Fig. 2, l. A linear approximation, $U_j = const$, is ob-
148 tained. A negligible current is found around point 1, and a surface current
149 estimate of about 1.7 m/s is found for point 2.

150 Planes ($F - F_0$) for these two image fragments are presented in Fig. 2, g,

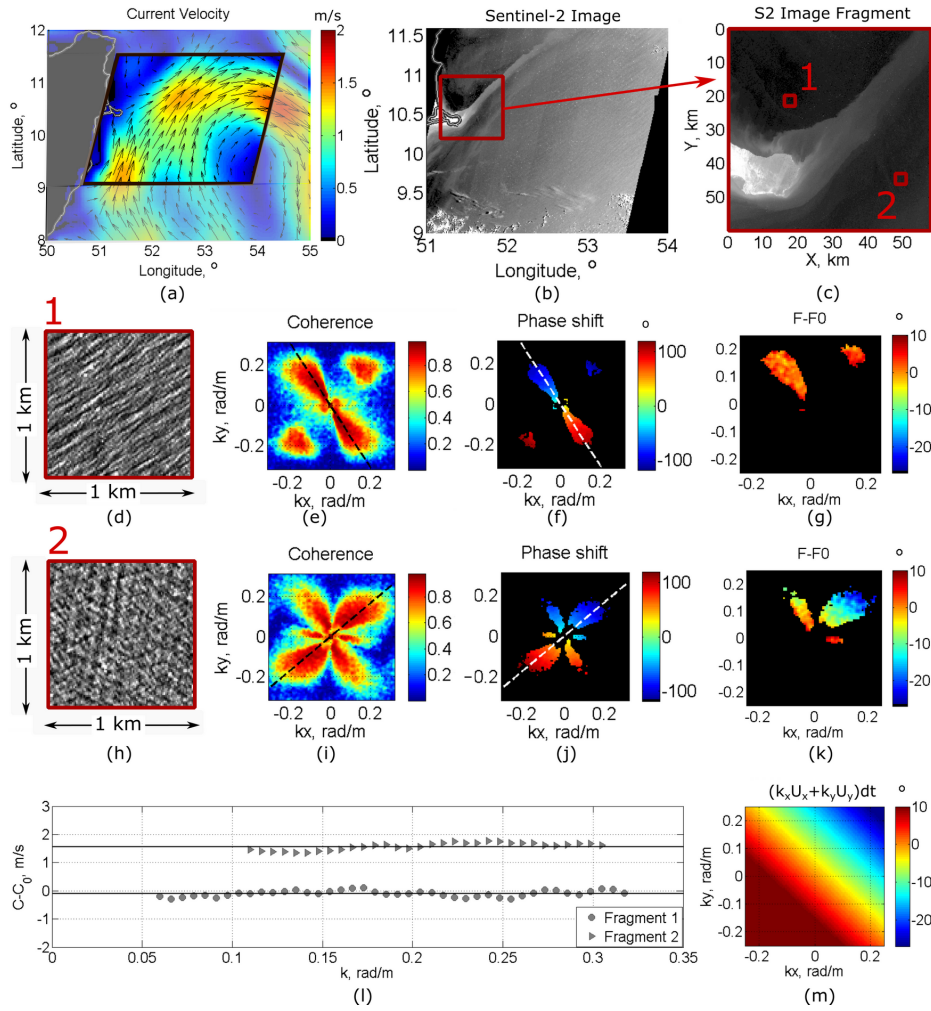


Figure 2: (a) Current field on 2016-08-27 near Somalia according to altimeter data; (b) MSI Sentinel-2 image, obtained on 2016-08-27, 06:46; (c) image fragment with current front manifestation; (d) zoomed image fragment around point 1; (e) coherence for bands B02 and B04; (f) phase shift spectrum; (g) observed and theoretical phase difference; (h-k) the same as (d)-(g) but for fragment 2; (l) current velocity retrieval for the directions marked with dashed lines in (f) and (j); (m) plane approximation of $(F - F_0)$ plotted in (k).

151 k. The distribution of $F - F_0$ is almost uniform and close to zero for the point
152 outside the current. It is significantly inclined in the second case. Using the
153 least square method (Fig. 2, m) to retrieve the phase plane, the corresponding
154 values of current components are $U_x = 1.26$ m/s and $U_y = 1.19$ m/s.

155 **3. Results**

156 *3.1. Ocean Surface Current*

157 Repeated over other image fragments, where waves are clearly distin-
158 guished, this procedure helps to reconstruct a current field throughout the
159 satellite observation areas. As obtained, the resulting current field, shown
160 in Fig. 3, a, is in a good qualitative agreement with altimeter derived esti-
161 mates, Fig. 2, a, and the detected large scale brightness features tracing the
162 current front location, Fig. 2, b. Quantitative comparisons are presented in
163 Fig. (3), b, c. Respective correlation coefficients, given in figure titles, show
164 high statistical significance of the result. Both retrieved current amplitude
165 and direction variability generally follow altimeter-derived estimates. The re-
166 trieved flow is stronger than the time- and spatial-averaged altimeter derived
167 one. This “overestimation” is also systematic for the other cases considered
168 below. Besides some isolated false points, an artificial strip-like structure
169 is apparent in Fig. 3, a. This is an indication of a small systematical error
170 inside images taken from different clusters. This error can arise from both
171 inter-band geolocation inaccuracy and the time lag estimate. As further an-
172 alyzed in Section 4, the former factor is the most significant for Sentinel-2
173 images.

174 Examples of surface current reconstruction over other ocean regions, the

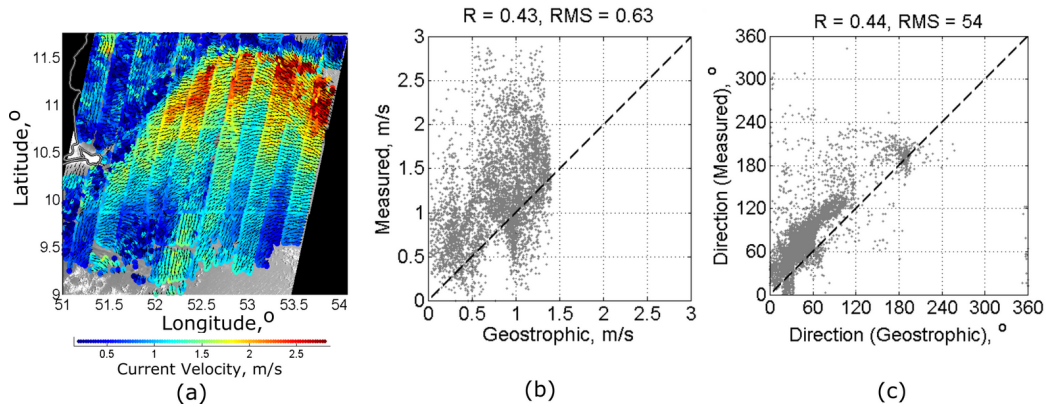


Figure 3: Current field retrieved from Sentinel-2 bands B02 and B04 for the case from Fig. 2 (a) and scatter plots of measured versus geostrophic current velocity (b) and direction (c).

175 Great Agulhas current system and the Gulf of Mexico, are further reported
 176 on Fig. 4. Again, at large scales, all retrieved current fields (Fig. 4, b)
 177 agree well with altimeter-derived geostrophic currents, (Fig. 4, a). At small
 178 spatial scales, the Sentinel-2 observations evidently capture more detailed
 179 structure and larger magnitudes in the main current core. This methodology
 180 essentially builds on spectral analysis of image brightness, and thus contem-
 181 poraneously provides surface wave spectral information, i.e. peak wavelength
 182 and direction at every point. Retrieved wave fields are presented in Fig. 4,
 183 right. Although all analyzed cases correspond to multi-modal wave situa-
 184 tions, an expected decrease/increase of the wavelength (with a correspond-
 185 ing increase/decrease of the wave amplitudes) of the same detected system,
 186 traveling opposite/along the current, is observed, i.e. comparison Fig. 4, b-
 187 c. This is indicating strong wave-current interactions (Ardhuin et al., 2017;
 188 Quilfen et al., 2018).

189 As Fig. 3, scatter plots of measured vs altimeter-derived geostrophic cur-

190 rent characteristics are presented in Fig. 4, d, e. Again, for the current
191 magnitude, correlation coefficients are high (> 0.7), while retrieved currents
192 are biased towards higher values, especially in the current core. Compare
193 solid and dashed lines in Fig. 3, d, left, where all points and only points
194 with $U < 2$ m/s are taken, respectively. For the current direction, Fig. 3, e,
195 correlation coefficients are less significant due to small angle variability. Still,
196 estimates aggregate around the mean line, indicating the likely correctness
197 of reconstructed directions.

198 *3.2. Bathymetry*

199 Another Sentinel-2 image, overlapping an intense current region, is re-
200 ported on Fig. 5. This snapshot contains a part of the Gulf Stream, and
201 was acquired on 2016-05-14, 15:59, over the Florida shelf Atlantic region.
202 The part of the current field covered by the MSI image is consistent with
203 altimeter-derived estimates, Fig. 5, a, d, e. The current frontal location is
204 well-delineated and matches both altimeter gradients and brightness peculiar-
205 ities on optical image (not shown). In line with previous results, the retrieved
206 current is slightly stronger than the altimeter-derived one. Analysis also re-
207 veals an uniform flow of about 0.5 m/s, detected towards East-Southeast,
208 probably associated to the tidal current, and thus not present in altimeter
209 products.

210 In the shelf area, the total dispersion relation, accounting for the water
211 depth, must be considered, Eq. (5), to estimate the flow velocity. Indeed, as
212 obtained from Fig. 5, b, the waves traveling from the East are significantly
213 modified by the bottom topography, shortening from 120 m in the East to 80
214 m at the coast. This measurable effect can help to solve the inverse problem,

215 i.e. to estimate the ocean depth through Eq. (7). As anticipated, Fig. 5, c, f,
216 display very good agreement of the reconstructed bathymetry and ETOPO1
217 Global Relief Model (www.ngdc.noaa.gov/mgg/global/).

218 3.3. *Small scale surface current*

219 All above examples confirm an overall qualitative agreement with large-
220 scale altimeter-derived estimates. As understood, these medium-resolution
221 products cannot be used to evaluate detected fine structures of the retrieved
222 current fields. A case, reported in Fig. 6, typically encompass large spatial
223 variability of the surface current at small scales. Sentinel-2 MSI image was
224 acquired on April, the 3rd 11:33, in North-East Atlantic, a region with intense
225 tidal currents. MARC model (Modeling and Analysis for Coastal Research,
226 <http://marc.ifremer.fr/en/results/currents/>), Fig. 6, a, forecasts currents up
227 to 3 m/s, over the North-North-East part, around Ouessant Island, at the
228 time of the acquisition. Strong current variability at small scales, $O(1000$
229 $m)$, is seemingly recovered with the proposed method, Fig. 6, b. Again,
230 when results in neighbor strips systematically differ, it is likely indicating
231 inter-channel geolocation imperfection in one or both clusters.

For more in-depth analysis, the accuracy of current reconstruction can be indirectly controlled by checking the expected frequency conservation law, following from kinematic equations for wave rays in the geometrical optics approximation (e.g. Phillips (1977)):

$$\omega = \omega_0 + \mathbf{k}\mathbf{U} = \text{const}, \quad (8)$$

232 where $\omega_0 = \sqrt{gk \tanh(kh)}$ is the wave intrinsic frequency of surface water
233 waves and ω is the detected frequency of the surface gravity wave propagating

234 in a current region.

235 As obtained and reported on Fig. 6, c, ω_0 , estimated from the brightness
236 peak wavenumber, strongly fluctuates in the region of intense non-uniform
237 current. On the opposite, the total frequency $\omega_0 + \mathbf{k}\mathbf{U}$, Fig. 6, d, is much
238 smoother, in line with the current field reconstruction.

239 Differentiation of Eq. (8) reduces it to one-dimensional expressions, elim-
240 inating the unknown constant:

$$\begin{aligned} -d\omega_0/dx &= d(k_x U_x + k_y U_y)/dx \\ -d\omega_0/dy &= d(k_x U_x + k_y U_y)/dy, \end{aligned} \quad (9)$$

In terms of wave-ray trajectories, an interesting consequence of these kinematic equations is the expected relation between the radius of curvature R of the wave-rays, the wave group velocity c_g and the vertical component of the current vorticity, assuming $c_g \gg U$ (Kenyon, 1971):

$$c_g/R = (\text{rot}\mathbf{U})_z. \quad (10)$$

241 Both Eq. (9) and Eq. (10) can then be used to check the validity of all
242 retrieved current fields. U and ω_0 derivatives can be estimated, using a least
243 square method inside areas encompassing sufficient number of points, to en-
244 sure reliable surface current estimates. Ray curvature is estimated following
245 the same procedure, through the derivatives of the wave vector direction α :

$$\frac{1}{R} = \frac{\partial\alpha}{\partial r} = \frac{\partial\alpha}{\partial x} \cos\alpha + \frac{\partial\alpha}{\partial y} \sin\alpha. \quad (11)$$

246 The comparison between left and right parts of Eq. (9) and Eq. (10), for
247 the cases shown in Fig. 3 and Fig. 4, is presented Fig. 7. Mean values of

248 each parameter (gray dots) are calculated around every point inside small
249 0.2° square image fragments. Results first appear highly scattered. This
250 is mainly induced from unstable estimations of the derivatives and their
251 combinations from spatially non-uniform fields. This is especially evident
252 for cases with multiple wave systems for which the chosen wavenumber peak
253 may belong to any of co-existing wave trains. The ray curvature is also very
254 sensitive and difficult to evaluate (Eq. (11), Fig. 7, bottom) given the small
255 dynamic range of wave direction values inside each squared area. Yet, bin-
256 averaging (magenta/purple squares) improves estimates, close to the mean
257 expected one-to-one line (black). Overall, the retrieved current fields are thus
258 generally consistent with the conservation law principle.

259 *3.4. Whitecap Velocities*

260 To further take advantage of the time-lagged Sentinel-2 MSI acquisitions,
261 the direct displacements of moving coherent targets can also be performed.
262 For ocean applications, a 1-s time-lag is sufficient to study motion and pe-
263 riodicity of whitecaps forming during wave breaking events (Donelan et al.,
264 1972). In the example shown Fig. 8, upper line, fragments from different
265 parts of the Sentinel-2 observations, considered in Fig. 2 and Fig. 3 (Somali),
266 are combined to construct RGB-images. The red color corresponds to the ini-
267 tial signal, i.e. adjusted B02 or B04 brightness. The green color corresponds
268 to the same signal, acquired 1 s latter. The blue color corresponds to the
269 averaged signal. Whitecaps are usually smaller than Sentinel-2 pixel resolu-
270 tion (10 m), but wave breaking events are clearly detected. Motions of wave
271 breaking fronts can then be obtained. Inter-channel correlation function pro-
272 vides object displacement and thus, their velocity and direction (Kubryakov

273 et al. (2018)). Peak positions of the resulting correlation functions, shown
274 in Fig. 8, f-j, correspond to the mean direction of the whitecap propagation.
275 The estimated velocities range between 5 m/s and 8 m/s, comparable to the
276 phase and group velocities of the dominant waves, about 9 m/s and 4.5 m/s,
277 respectively.

278 **4. Discussion: Method Applicability and Accuracy**

279 This methodology to infer surface current velocity shall apply to any
280 space-borne optical multi-channel images, having inter-channel time-lag of
281 order of seconds, and sufficient spatial resolution to resolve surface waves.
282 A necessary condition is indeed the visibility of surface wave modulations
283 to analyse their propagation properties. With pixel resolution of order 10
284 m, this is usually fulfilled in most of the sun glint area. Except within
285 the very specular part of the glint or too far from it, surface waves are
286 well detected. Other factors can prevent the analysis of wave dispersion
287 characteristics: clouds, surface roughness features like slicks, ship tracks or
288 objects on the sea surface, including bright whitecaps. Whitecaps are often
289 present in frontal current regions, and not solely during windy conditions.
290 Yet, the methodology appears quite robust. As demonstrated, Fig. 3 and
291 Fig. 7, a (Somali case), a surface current field was retrieved under high wind
292 conditions with numerous detectable whitecaps. The retrieved current values
293 may then be overestimated over the most active wave breaking area (North-
294 East part). Future investigations shall thus be necessary to better assess
295 possible biases induced by visible whitecaps.

296 Results also depend on the directional spread of the wave spectrum, and

297 the relative wave-current direction. Waves propagating perpendicular to a
 298 current direction are only weakly impacted. The procedure described in
 299 Section 2 can not apply. Ideally, wave systems exhibiting a large directional
 300 spread will help. Technically, a solution is to design an instrument with
 301 increased multi-angle bi-static detector capability, to combine high angular
 302 sampling with high spatial resolution (Rascle et al. (2018)).

303 Accurate estimation directly depends on the time-lag between acqui-
 304 sitions, and their co-registration error. To retrieve surface wave propagation
 305 characteristics, time-lags should be long enough to provide a reliable cross-
 306 spectral phase estimate, but short enough to ensure strong coherency between
 307 the two consecutive observations. For a time shift dt and displacement dx ,
 308 with systematic errors Δt and Δx , respectively, the velocity estimate error
 309 is

$$\Delta v = v - \frac{vdt + \Delta x}{dt + \Delta t} = v \frac{\Delta t}{dt + \Delta t} - \frac{\Delta x}{dt + \Delta t}. \quad (12)$$

310 The first term in (12) r.h.s. indicates the time-lag uncertainty. The
 311 second one is the image co-registration error. Time-lag uncertainty increases
 312 with decreasing dt , i.e. the larger the time-lag the better the accuracy of the
 313 velocity estimation. Though not equivalent, spatial and temporal errors can
 314 occasionally compensate each other: a systematic displacement will appear as
 315 an additional current. A constant $\Delta x/dt$ adds to the estimated phase velocity
 316 $c(k)$, and thus to the respective current projection. A temporal error distorts
 317 $c(k)$ with a coefficient $dt/(dt + \Delta t)$. The influence of both terms in (12) is
 318 shown in Fig. 9, for 1 s and 2 s inter-band time-lags. For the bands with 10
 319 m resolution and 1 s time-lag, a co-registration accuracy better than 0.1 m

320 (0.01 pixel) is required to ensure reliable velocity estimate, down to 0.1 m/s.
321 Examples in Section 3 demonstrate that surface currents down to 0.3 m/s
322 are correctly retrieved, except for the case shown on Fig. 6. For this case,
323 the current magnitudes from neighbor strips systematically differ by about
324 1 m/s. Accordingly, B02-B04 inter-band matching accuracy is better than
325 0.1 pixel, and for most cases, better than 0.03 pixel. MSI co-registration
326 accuracy seems to outclass the values listed in the Sentinel-2 data quality
327 report, where 0.168 pixel is stated for B02 and B04 (sentinel.esa.int).

328 Increasing the time-lag reduces the error (green line). But, a 5% time-lag
329 error leads to 0.5 m/s uncertainty in velocity estimate for 50 m waves. In
330 our present analysis, dt has been estimated with an accuracy of about 1%
331 (Section 2). The associated error is then negligible compared to the error
332 related with co-registration precision.

333 5. Conclusion

334 Satellite sun glint images of the sea surface often provide highly power-
335 ful means to observe and quantify small-scale spatial variations of currents,
336 wind and surfactants. In this paper, the Sentinel-2 MultiSpectral Instrument
337 properties and capabilities are further demonstrated.. Sentinel-2 instruments
338 collect multiple spectral band images, corresponding to specific sensing wave-
339 length and spatial resolution, i.e. 10 m, 20 m, and 60 m. Because images are
340 acquired one at the time, with a fixed time-lag between observations, spatio-
341 temporal characteristics of propagating ocean surface waves can uniquely be
342 retrieved, including motions of whitecaps.

343 A method is applied to estimate the surface current from images of the sea

344 surface, taken from two particular Sentinel-2 bands with a time delay of order
345 1 second. The measured deviation from the expected linear surface wave
346 dispersion relationship directly relates to surface current impacts. The wave-
347 rays, waveevenumber and dispersion fields, $w(\mathbf{k})$, can cover a fairly wide range
348 of angles to serve the reconstruction of the total surface current vector. In the
349 absence of current, and shallow water conditions, the dispersion variations
350 are determined by the ocean depth variations.

351 For MSI, the largest time-lag between acquisitions using 10-m resolution
352 bands, is of order 1 s. To improve surface current determination, optimized
353 acquisitions could consider video-like acquisitions, rather than two snapshots.
354 Already, the reconstructed current fields appear valuable. In absence of
355 ground-truth information, results well compare, at large to medium spa-
356 tial scales, with altimeter-derived geostrophic current estimates. At higher
357 resolution, the analysis satisfy conservation laws, as obtained from wave-ray
358 kinematic equations.

359 The possibility to estimate the speed and direction of large whitecaps,
360 has also been tested. Again, this is opening for future investigations, as a
361 potential key capability to infer direct measurements of momentum and gas
362 fluxes.

363 As discussed for reliable current reconstruction, MSI images should be
364 co-registered with an accuracy better than 0.03 pixel. For Sentinel-2 MSI
365 measurements, this is generally fulfilled.

366 Overall, these different results demonstrate very encouraging prospects
367 to combine different satellite measurements (altimeter, optical, radar). The
368 design of dedicated future satellite missions to precisely retrieve surface cur-

369 rents at high resolution, may thus build upon a satellite constellation, build-
370 ing from standard altimeter data, to medium resolution measurements (fu-
371 ture SWOT mapping altimeter), completed with multi-angle bi-static optical
372 measurements (Kudryavtsev et al. (2012); Rascle et al. (2018)). Combining
373 high angular diversity and pixel spacing, multi-angle optical measurements
374 could also include polarization capabilities to help separate sunglint radi-
375 ance from water-leaving, skyglint, and whitecap contributions (Harmel and
376 Chami (2013)). While limited to favorable day-light and cloud-less condi-
377 tions, Sentinel-2 MSI observations already offer essential means for multi-
378 validation purposes: local wind, waves and current transformations and in-
379 teractions. Future investigations are necessary to better assess biases, pos-
380 sibly induced by detected whitecaps. To note, the combined capability to
381 track whitecaps and surface wave field transformation shall also further be
382 explored to map and inform complex wave-current interactions (Rascle et al.
383 (2014); Ardhuin et al. (2017)) in the vicinity of ocean fronts and coastal
384 areas.

385 **Acknowledgments**

386 The authors are grateful to Vladimir Dulov for the discussion and useful
387 comments, and to anonymous Reviewers whose valuable suggestions helped
388 to improve the paper. The work was supported by Russian Science Foun-
389 dation via grant 17-77-30019 and the Ministry of Education and Science of
390 the Russian Federation under the State Assignment No. 0827-2018-0003, also
391 supported through the ESA projects SARONG under contract 4000117644/16/NL/FF/gp
392 and GlobCurrent under contract 4000109513/13/ILG. The Copernicus Sen-

393 tinel2 data used in this paper are available at: <https://scihub.copernicus.eu/dhus/#/home>

394 **References**

395 Ardhuin, F., Gille, S. T., Menemenlis, D., Rocha, C. B., Rasche, N., Chapron,
396 B., Gula, J., and Molemaker, J. (2017). Small-scale open ocean currents
397 have large effects on wind wave heights. *Journal of Geophysical Research:*
398 *Oceans*, 122(6):4500–4517.

399 Barber, N. F. (1949). A Diffraction Analysis of a Photograph of the Sea.
400 *Nature*, 164(485).

401 Chapron, B., Collard, F., and Ardhuin, F. (2005). Direct measurements of
402 ocean surface velocity from space: Interpretation and validation. *Journal*
403 *of Geophysical Research: Oceans*, 110(C7).

404 De Michele, M., Leprince, S., Thiebot, J., Raucoules, D., and Binet, R.
405 (2012). Direct measurement of ocean waves velocity field from a single
406 spot-5 dataset. *Remote Sensing of Environment*, 199:266–271.

407 Donelan, M., Longuet-Higgins, M. S., and Turner, J. S. (1972). Periodicity
408 in whitecaps. *Nature*, 239(5373):449–451.

409 Dugan, J. and Piotrowski, C. (2003). Surface current measurements us-
410 ing airborne visible image time series. *Remote Sensing of Environment*,
411 84:309–319.

412 Dugan, J. P., Piotrowski, C. C., and Williams, J. Z. (2001). Water depth
413 and surface current retrievals from airborne optical measurements of sur-

414 face gravity wave dispersion. *Journal of Geophysical Research: Oceans*,
415 106(C8):16903–16915.

416 Fedele, F., Benetazzo, A., Gallego, G., Shih, P.-C., Yezzi, A., Barbariol, F.,
417 and Ardhuin, F. (2013). Space-time measurements of oceanic sea states.
418 *Ocean Modelling*, 70:103–115.

419 Goldstein, R. and Zebker, H. (1987). Interferometric radar measurement of
420 ocean surface currents. *Nature*, pages 707–709.

421 Hansen, M., Kudryavtsev, V., Chapron, B., Johannessen, J., Collard, F.,
422 Dagestad, K.-F., and Mouche, A. (2012). Simulation of radar backscatter
423 and doppler shifts of wave-current interaction in the presence of strong
424 tidal current. *Remote Sensing of Environment*, 120:113 – 122. The Sentinel
425 Missions - New Opportunities for Science.

426 Harmel, T. and Chami, M. (2013). Estimation of the sunglint radiance
427 field from optical satellite imagery over open ocean: Multidirectional ap-
428 proach and polarization aspects. *Journal of Geophysical Research: Oceans*,
429 118(1):76–90.

430 Johannessen, J. A., Chapron, B., Collard, F., Kudryavtsev, V., Mouche, A.,
431 Akimov, D., and Dagestad, K.-F. (2008). Direct ocean surface velocity
432 measurements from space: Improved quantitative interpretation of envisat
433 asar observations. *Geophysical Research Letters*, 35(22).

434 Kääb, A., Lamare, M., and Abrams, M. (2013). River ice flux and water
435 velocities along a 600 km-long reach of lena river, siberia, from satellite
436 stereo. *Hydrology and Earth System Sciences*, 17(11):4671–4683.

- 437 Kääb, A. and Leprince, S. (2014). Motion detection using near-simultaneous
438 satellite acquisitions. *Remote Sensing of Environment*, 154:164–179.
- 439 Kenyon, K. E. (1971). Wave refraction in ocean currents. *Deep Sea Research*
440 *and Oceanographic Abstracts*, 18(10):1023 – 1034.
- 441 Kubryakov, A., Plotnikov, E., and Stanichny, S. (2018). Reconstructing
442 large- and mesoscale dynamics in the black sea region from satellite im-
443 agery and altimetry data. a comparison of two methods. *Remote Sensing*,
444 10(2).
- 445 Kudryavtsev, V., Myasoedov, A., Chapron, B., Johannessen, J. A., and Col-
446 lard, F. (2012). Imaging mesoscale upper ocean dynamics using synthetic
447 aperture radar and optical data. *Journal of Geophysical Research: Oceans*,
448 117(C4):n/a–n/a. C04029.
- 449 Kudryavtsev, V., Yurovskaya, M., Chapron, B., Collard, F., and Donlon,
450 C. (2017a). Sun glitter imagery of ocean surface waves. Part 1: Direc-
451 tional spectrum retrieval and validation. *Journal of Geophysical Research:*
452 *Oceans*, 122(2):1369–1383.
- 453 Kudryavtsev, V., Yurovskaya, M., Chapron, B., Collard, F., and Donlon,
454 C. (2017b). Sun glitter imagery of surface waves. Part 2: Waves trans-
455 formation on ocean currents. *Journal of Geophysical Research: Oceans*,
456 122(2):1384–1399.
- 457 Leckler, F., Ardhuin, F., Peureux, C., Benetazzo, A., Bergamasco, F., and
458 Dulov, V. (2015). Analysis and Interpretation of Frequency–Wavenumber

- 459 Spectra of Young Wind Waves. *Journal of Physical Oceanography*,
460 45(10):2484–2496.
- 461 Martin, A. C. and Gommenginger, C. (2017). Towards wide-swath high-
462 resolution mapping of total ocean surface current vectors from space: Air-
463 borne proof-of-concept and validation. *Remote Sensing of Environment*,
464 197:58 – 71.
- 465 Martin, A. C., Gommenginger, C. P., and Quilfen, Y. (2018). Simultaneous
466 ocean surface current and wind vectors retrieval with squinted sar inter-
467 ferometry: Geophysical inversion and performance assessment. *Remote*
468 *Sensing of Environment*, 216:798 – 808.
- 469 Matthews, J. and Awaji, T. (2010). Synoptic mapping of internal-wave mo-
470 tions and surface currents near the lombok strait using the along-track
471 stereo sun glitter technique. *Remote Sensing of Environment*, 114(8):1765
472 – 1776.
- 473 Matthews, J. P. and Yoshikawa, Y. (2012). Synergistic surface current map-
474 ping by spaceborne stereo imaging and coastal hf radar. *Geophysical Re-*
475 *search Letters*, 39(17).
- 476 Phillips, O. M. (1977). *The Dynamics of the Upper Ocean*. Cambridge
477 University Press, New York, 2 edition.
- 478 Quilfen, Y., Yurovskaya, M., Chapron, B., and Ardhuin, F. (2018). Storm
479 waves focusing and steepening in the agulhas current: Satellite observa-
480 tions and modeling. *Remote Sensing of Environment*, 216:561 – 571.

- 481 Rascle, N., Chapron, B., Ponte, A., Ardhuin, F., and Klein, P. (2014). Surface
482 roughness imaging of currents shows divergence and strain in the wind
483 direction. *Journal of Physical Oceanography*, 44(8):2153–2163.
- 484 Rascle, N., Molemaker, J., Marie, L., Nougier, F., Chapron, B., Lund, B.,
485 and Mouche, A. (2017). Intense deformation field at oceanic front inferred
486 from directional sea surface roughness observations. *Geophysical Research*
487 *Letters*, 44(11):5599–5608. 2017GL073473.
- 488 Rascle, N., Nougier, F., Chapron, B., and Ocampo-Torres, F. J. (2018).
489 Sunlight images of current gradients at high resolution: Critical angle and
490 directional observing strategy. *Remote Sensing of Environment*, 216:786 –
491 797.
- 492 Rebecq, H., Gallego, G., Mueggler, E., and Scaramella Perez, D. (2017).
493 Emvs: Event-based multi-view stereo - 3d reconstruction with an event
494 camera in real-time. *International Journal of Computer Vision*, pages 1–
495 21.
- 496 Rodriguez, E., Wineteer, A., Perkovic-Martin, D., Gál, T., Stiles, B., Ni-
497 amsuwan, N., and Rodriguez Monje, R. (2018). Estimating ocean vector
498 winds and currents using a Ka-band pencil-beam doppler scatterometer.
499 10. 576.
- 500 Romeiser, R., Runge, H., Suchandt, S., Kahle, R., Rossi, C., and Bell, P. S.
501 (2014). Quality assessment of surface current fields from terrasar-x and
502 tandem-x along-track interferometry and doppler centroid analysis. *IEEE*
503 *Transactions on Geoscience and Remote Sensing*, 52(5):2759–2772.

- 504 Takasaki, K., Sugimura, T., and Tanaka, S. (1994). Speed vector measure-
505 ment of moving objects using jers-1/ops data. *Journal of The Remote*
506 *Sensing Society of Japan*, pages 213–219.
- 507 Yurovskaya, M., Kudryavtsev, V., S. Shirokov, A., and Yu. Nadolya, I.
508 (2018a). Field measurements of the sea surface wave spectrum from pho-
509 tos of sunglitter taken from drone. *Sovremennye problemy distantsionnogo*
510 *zondirovaniya Zemli iz kosmosa*, 15:245–257.
- 511 Yurovskaya, M., Kudryavtsev, V. N., Chapron, B., Rascle, N., and Collard,
512 F. (2018b). Wave spectrum and surface current retrieval from airborne and
513 satellite sunglitter imagery. In *2018 IEEE International Geoscience and*
514 *Remote Sensing Symposium, IGARSS 2018, Valencia, Spain, July 22-27,*
515 *2018*, pages 3192–3195.
- 516 Yurovskaya, M., Rascle, N., Kudryavtsev, V., Chapron, B., Marié, L., and
517 Molemaker, J. (2018). Wave spectrum retrieval from airborne sunglitter
518 images. *Remote Sensing of Environment*, 217:61–71.
- 519 Yurovsky, Y. Y., Kudryavtsev, V. N., Grodsky, S. A., and Chapron, B.
520 (2019). Sea surface ka-band doppler measurements: Analysis and model
521 development. *Remote Sensing*, 11(7).

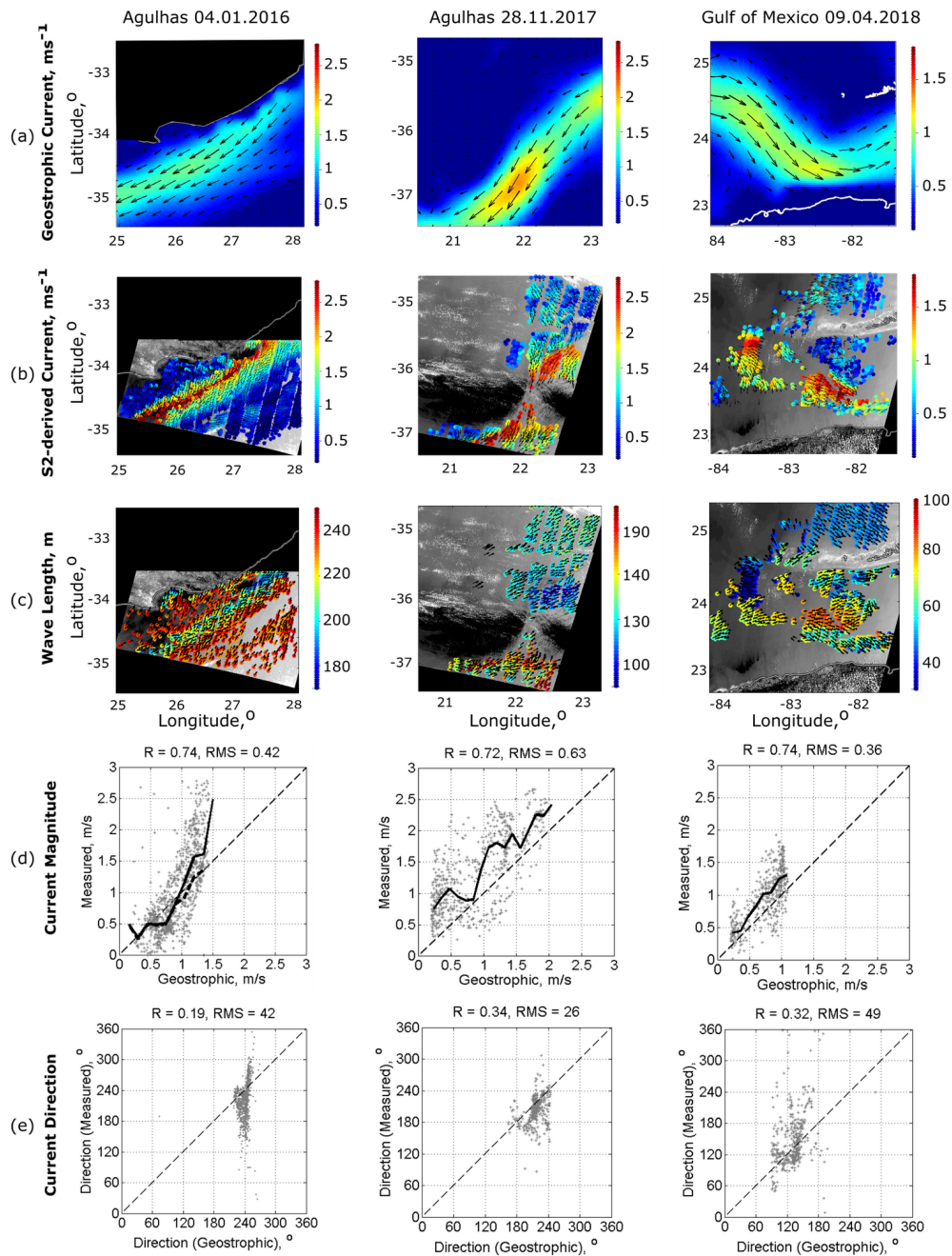


Figure 4: (a) Geostrophic current from altimeter data in the region of Agulhas current on the 4th of January, 2016 (left) and 28th of November, 2017 (center), and the Gulf of Mexico on 2018-04-09 (right); (b) respective surface currents retrieved from Sentinel-2 MSI images; (c) wavelengths and directions reconstructed from brightness spectra peak wavenumber; (d)-(e) scatter plots of measured versus geostrophic current velocity and direction (black solid lines show interval-averaged values, dashed line in (d), left, is the same, but for points $U < 2$ m/s).

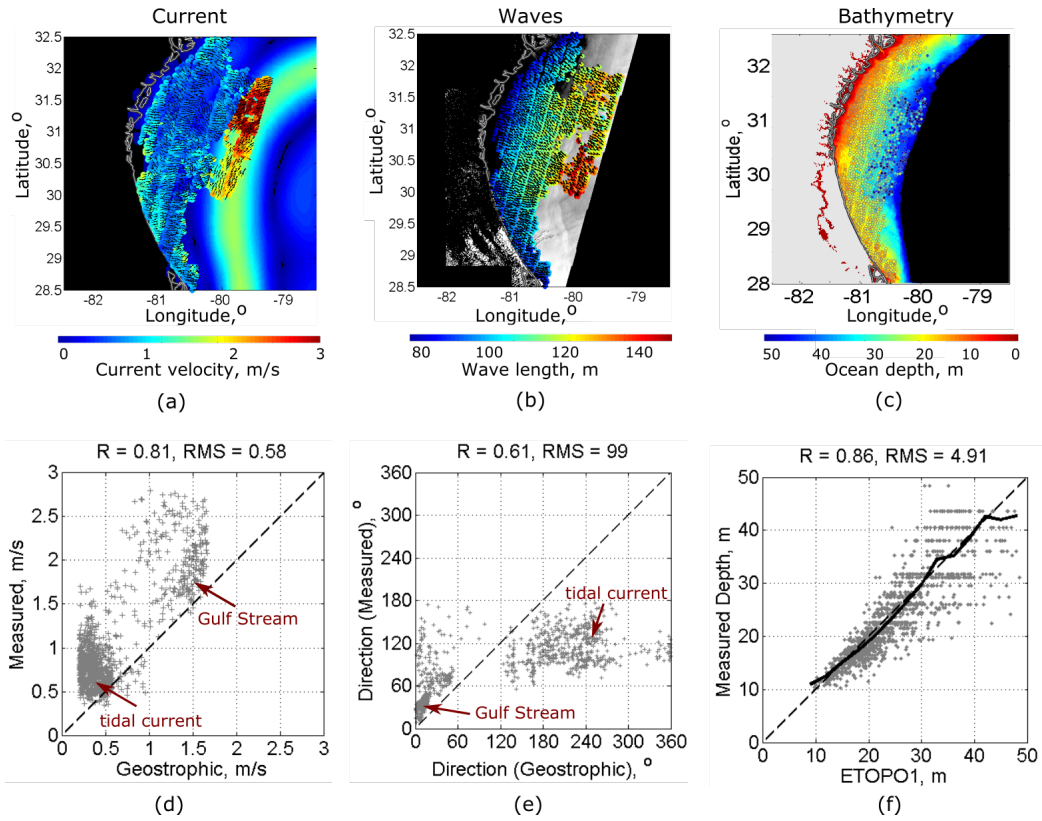


Figure 5: (a) MSI-derived current field (points with arrows) overlapping geostrophic current field in West Atlantic on the 14th of May, 2016; (b) wavelengths and directions obtained from Sentinel-2 image brightness; (c) ocean depth reconstructed through the wave dispersion relation from MSI image (dots) and ETOPO1 data (background); (d)-(e) scatter plots of geostrophic vs measured current velocity and direction; (f) scatter plot of ETOPO1 bathymetry vs reconstructed ocean depth.

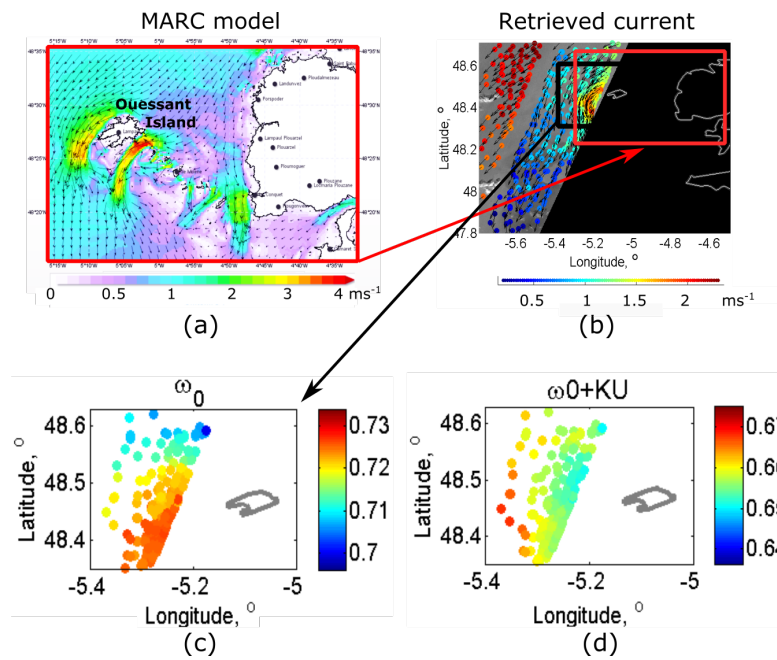


Figure 6: (a) Tidal current in the North of Biscay Bay on the 3rd of April, 11:30, according to MARC model; (b) current reconstructed from Sentinel-2 snapshot obtained on the 3rd of April, 11:33; (c) wave frequencies derived from image brightness spectra; (d) total wave frequency, $\omega_0 + kU$, calculated using MSI-derived current vectors.

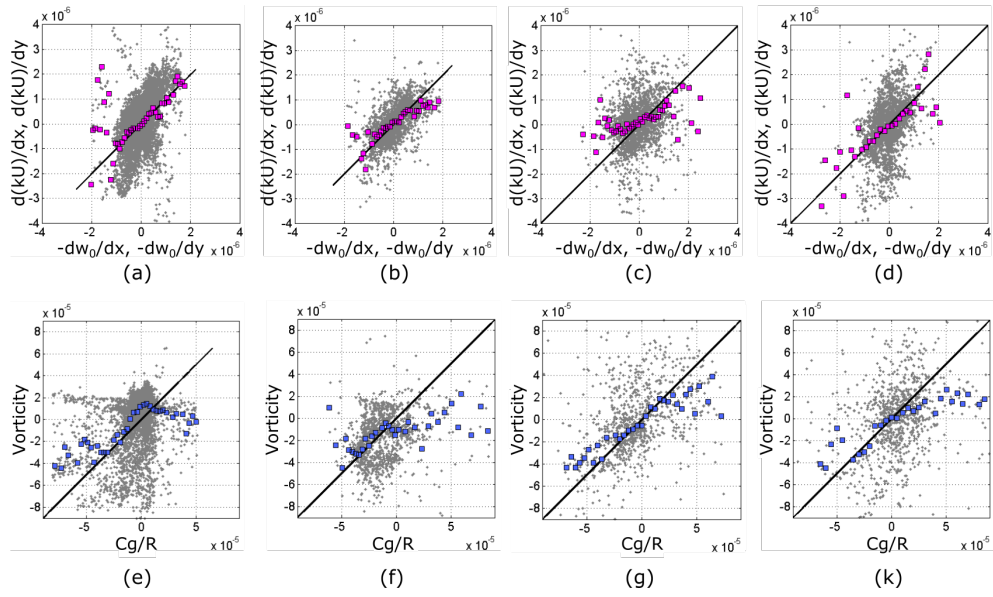


Figure 7: (a)-(d) left and right parts of Eq. 9 for every point (gray dots) in Fig. 3 and Fig. 4 (Somali current (a), Agulhas (b)-(c) and Gulf of Mexico (d)); squares are interval-averaged data; (e)-(k) left and right parts of Eq. 10 for the same cases as in (a)-(d).

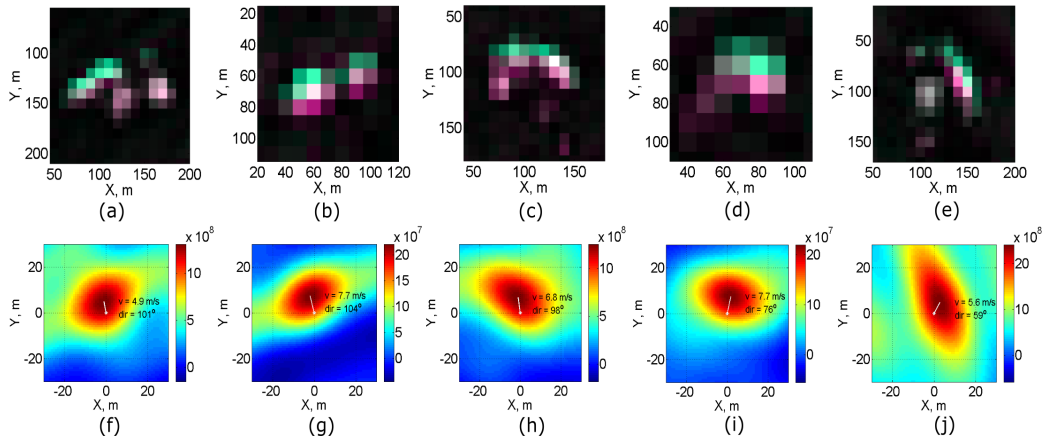


Figure 8: (a)-(e) RGB-compositions of MSI image fragments containing manifestation of wave breaking events. Red (earlier) and green (later) are the modified brightness signals of Sentinel-2 channels B02/B04, blue is their average, time lag is 1 s; (f)-(j) corresponding correlation functions; the location of maximum indicates event speed and direction.

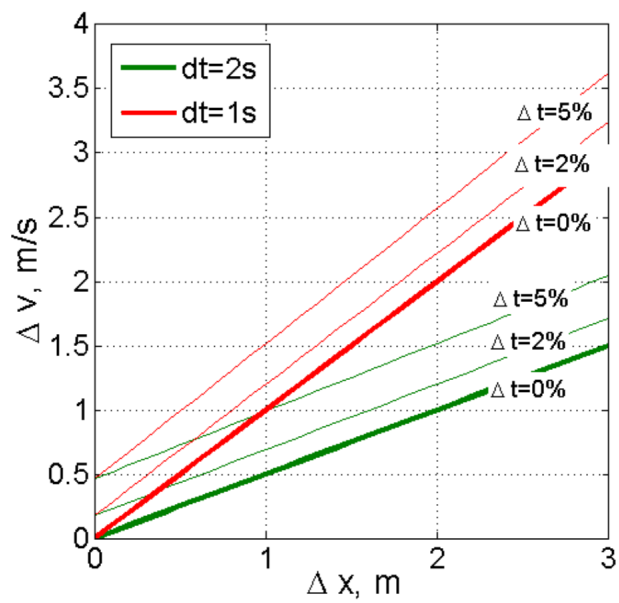


Figure 9: The absolute error of velocity estimate for 1 s and 2 s time lags (color) and different time lag estimation error Δt (for 50 m waves), and inter-channel matching accuracy Δx . Δx and Δt are of different signs here.